Journal of Science: Advanced Materials and Devices 8 (2023) 100611

Contents lists available at ScienceDirect

Journal of Science: Advanced Materials and Devices

journal homepage: www.elsevier.com/locate/jsamd

Original Article

^{63}Ni-based radioluminescent isotope cells with enhanced photon transport interfaces

Tongxin Jiang [a], Zan Ding [a], Renrong Zheng [a], Xiaobin Tang [b], Zhiheng Xu [b, **], Xin Li [c], Lifeng Zhang [c], Xue Li [c], Haisheng San [a, *]

[a] Pen-Tung Sah Institute of Micro-Nano Science and Technology, Xiamen University, Xiamen, 361005, China
[b] Department of Nuclear Science and Technology, Nanjing University of Aeronautics and Astronautics, Nanjing, 211106, China
[c] China Institute of Atomic Energy, Beijing, 102413, China

ARTICLE INFO

Article history:
Received 25 May 2023
Received in revised form
7 July 2023
Accepted 19 July 2023
Available online 22 July 2023

Keywords:
Radioluminescent
Isotope cell
Spin-coated ZnS:Cu
Metal reflective film

ABSTRACT

Radioluminescent isotope cells (RLICs) have the advantages of a long lifetime and high stability due to the use of phosphor material with excellent radiation resistance. Current research efforts mainly focus on the improvement of energy conversion efficiency. This study presents a ^{63}Ni-based RLIC with enhanced photon transport interfaces. The ZnS:Cu phosphor layer is spin-coated directly onto the surface of an AlGaInP-based photovoltaic cell (PC) to achieve efficient coupling of photons by optimizing the transmission interface, and a metal film is sputtered onto the ZnS:Cu layer to reflect radioluminescence towards the PC. Theoretical simulations and experiments are used to compare and validate the integration designs of the ZnS:Cu layer and metal reflective films (Ag, Al, and Ni). It is demonstrated that the RLIC based on the spin-coated ZnS:Cu/PC structure with a 100 nm thick Ag film can increase the output power by 52.6%, compared to conventional RLICs based on adhesive ZnS:Cu/BOPP/PC structure. Maximum efficiency of 0.92% is expected under beta radiation of ^{63}Ni. The enhancement of photon transport is attributed to fluorescence backward reflection and refractive index matching at the interfaces.

1. Introduction

Nuclear cells have the advantages of long life, strong stability, and high energy density [1–3], which have a huge potential for application in harsh environments, such as deep sea, space, polar regions and deserts [4–7]. Radioluminescent isotope cells (RLICs) can convert energy from radioactive decay into light using a phosphor material and then into electricity using a photovoltaic cell (PC) [8]. Compared to betavoltaic and alphavoltaic cells, which directly convert the radiation energy into electricity, RLICs have a longer lifetime due to the use of phosphor materials with higher radiation resistance than semiconductors [9–11]. However, the indirect energy conversion process results in a decrease in overall energy conversion efficiency (ECE). Therefore, research efforts related to RLICs are mainly focused on improving ECE [12–14] and reliability [15–17]. In previous work, the optimal matching of radioisotope sources and phosphor layers has been studied. Alpha-decay radioisotopes such as Americium-241 (^{241}Am), Polonium-210 (^{210}Po), and Plutonium-238 (^{238}Pu), exhibit high ionization energy, which can result in significant radiation damage to energy conversion materials [18]. As a result, these radioisotopes are rarely used as radiation sources for RLICs [19]. Gamma sources such as Cobalt-60 (^{60}Co) and Cesium-137 (^{137}Cs) generate high-energy electromagnetic radiation with higher penetration ability and, thus, lower energy deposition in energy conversion materials [20]. Hence, they are often combined with scintillation crystals [21,22] or used for irradiation aging experiments [23,24]. Considering the effective deposition of radiation energy and the stability of conversion materials, beta-decay radioisotopes are considered more suitable for RLICs [25]. Tritium-3 (^{3}H) has the advantages of super-high specific activity and low cost, but its average decay energy is relatively low at 5.7 keV [26,27]. Promethium-147 (^{147}Pm) has a higher average decay energy (62 keV) but a short half-life of only 2.6 years [28]. Therefore, neither is regarded as an ideal beta-radiation source. Strontium-90 (^{90}Sr) and Nickel-63 (^{63}Ni) have greater potential for application. In particular, ^{90}Sr has an average decay energy of 196 keV, with an energy deposition depth up to

* Corresponding author.
** Corresponding author.
E-mail addresses: xuzhiheng@nuaa.edu.cn (Z. Xu), sanhs@xmu.edu.cn (H. San).
Peer review under responsibility of Vietnam National University, Hanoi.

https://doi.org/10.1016/j.jsamd.2023.100611

millimeter-level in the fluorescent materials. It requires the design of phosphor layers with corresponding thicknesses, which would result in severe self-absorption loss of photons in such thick materials [29,30]. ZnS:Cu material can generate radioluminescence efficiently [31], but its fluorescence self-absorption (FSA) effect is significant due to its low transmittance [32]. Therefore, the ^{63}Ni radioisotope with a moderate average decay energy of 17.4 keV, can make maximum energy deposition at a micrometer-level depth (close to the powder particle size of fluorescent material) with the FSA effect as low as impossible. This makes it an ideal radiation source for achieving high ECE in RLICs [33].

The conventional RLIC typically uses a planar sandwich structure (Fig. 1 (a)) consisting of a radiation source, a phosphor layer on a transparent substrate, and a PC. There are two energy transport interfaces (the radiation source/phosphor layer interface and the phosphor layer/PC interface), which can cause significant fluorescence transport loss. Firstly, radioluminescent photons generated from the phosphor layer are emitted at a 4π space angle, but only the photons within a 2π half-space angle are incident on the PC. The other photons incident towards the radiation source cannot be collected and utilized, resulting in a radioluminescence energy loss of about 50%. Secondly, the radioluminescent photons must pass through the transparent substrate and an air interface medium before they can be collected by the PCs. In the photon transport process, the mismatch of refractivity between different transport media (e.g., low refractivity for transparent substrate and high refractivity for phosphor materials and PC materials) can induce serious photon reflection at the two interfaces, thereby diminishing the amount of fluorescence captured by PCs.

In this study, two approaches were adopted to enhance the fluorescence transport efficiency. On the one hand, the ZnS:Cu layer was spin-coated directly on the surface of PCs to weaken the interface photon reflection caused by the transparent substrate and air, as shown in Fig. 1(b). On the other hand, a metal film was deposited on the spin-coated ZnS:Cu to reflect the backward fluorescence towards the PCs, as shown in Fig. 1(c). The effects of the spin-coated phosphor layer and reflective metal film on the output power of RLICs were investigated both theoretically and experimentally. This novel interface structure design provides a new strategy for improving the ECE of RLICs.

2. Experiment

2.1. Materials and devices preparation

It has been demonstrated that the ZnS:Cu phosphor layer prepared on the surface of a Biaxially Oriented Polypropylene (BOPP) substrate using the adhesion method can match well with ^{63}Ni radiation source [17]. In this study, the RLIC is designed as an integrated structure, as shown in Fig. 1(c). The ZnS:Cu phosphor layer was directly spin-coated onto the surface of the PC, and then a reflective film was sputtered on top surface of ZnS:Cu layer. Then, a ^{63}Ni planar source was placed on top of the reflective film.

ZnS:Cu paste was prepared by mixing ZnS:Cu powder with a gel composed of Xylene (60%wt) and polymethyl methacrylate (PMMA) (40%wt). The ZnS:Cu paste was then spin-coated onto the surfaces of the PCs. To evaluate the optical performance of the spin-coated ZnS:Cu layer, the ZnS:Cu paste was also spin-coated onto a PMMA substrate to form the spin-coated ZnS:Cu/PMMA layer. For comparison, ZnS:Cu powder was adhered to a BOPP substrate to form the adhesive ZnS:Cu/BOPP layer. The AlGaInP-based PCs, which have a high external quantum efficiency (EQE) in the emission spectrum of ZnS:Cu phosphor, were used to convert the radioluminescence into electricity. Ag, Al and Ni were selected as the metal materials for the reflective films on the surface of the phosphor layer, respectively. Ag and Al are generally regarded as ideal candidate materials for preparing reflective layers. Ni was employed to verify the feasibility of using ^{63}Ni as both a radioactive and reflective layer. Magnetron sputtering (Denton, EXPLORER-14) was utilized to prepare the metal films on the surface of ZnS:Cu phosphor layer.

2.2. Characterization

The source meters (Keithley 2450 and Keithley 2636) were used to test electrical performance of devices in a dark Faraday cage. The radioluminescence (RL) spectrum of the adhesive and spin-coated ZnS:Cu layer was measured by fluorescence spectrophotometer (Agilent, Cary Eclipse). The photoluminescence (PL) spectrum of the spin-coated phosphor layer with different metal films was measured using another fluorescence spectrophotometer (HITACHI, F-7000). The morphologies of the spin-coated and adhesive ZnS:Cu layers were characterized by scanning electron microscopy (Zeiss, SUPRA55 SAPPHIRE).

3. Results and discussion

Fig. 2(a) and (b) show the photos of the PC before and after spin-coating with the ZnS:Cu layer. The thickness of the spin-coated ZnS:Cu layer was measured to be around 15 μm when using a spin-coating speed of 2000 rpm/5 s, 5000 rpm/10 s, and 10,000 rpm/200 s, successively, which matches the energy deposition depth of ^{63}Ni simulated using the Monte Carlo (MC) method. Fig. 2(c) shows a partial SEM image of the junction of the spin-coated ZnS:Cu and PC. It can be observed that the spin-coated ZnS:Cu layer was closely attached to the top surface of the PC,

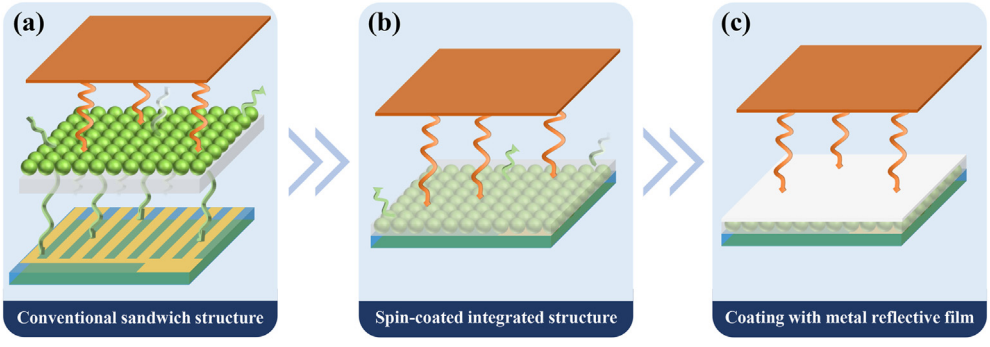

Fig. 1. Schematic diagrams of three types of RLIC structures. (a) Conventional sandwich structure. (b) Spin-coated integrated structure. (c) Spin-coated integrated structure with reflective film.

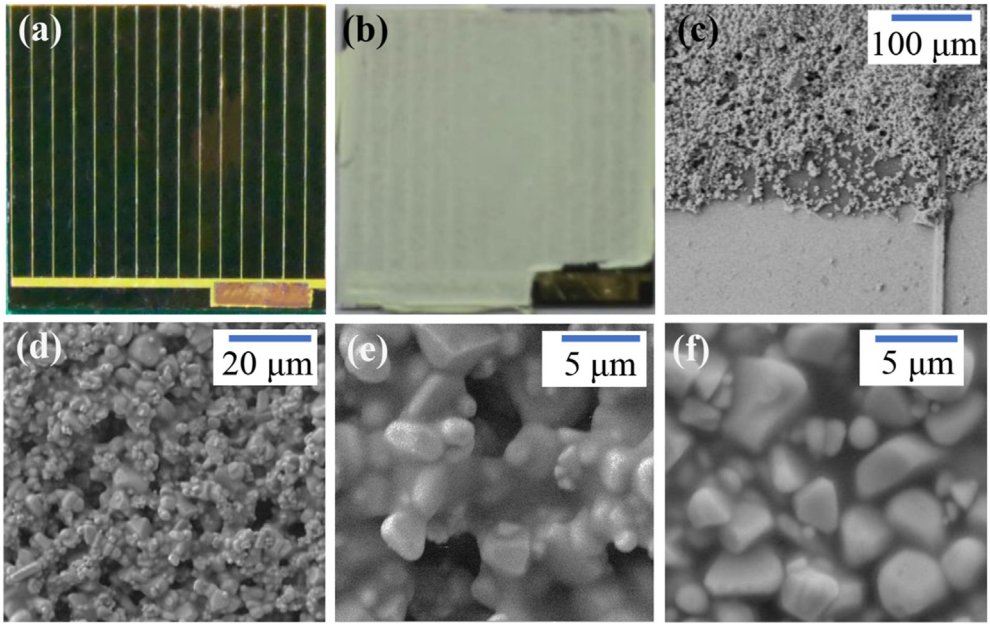

Fig. 2. Photos of the (a) PC and (b) spin-coated ZnS:Cu/PC structure. Partial SEM images of (c) the junction of the spin-coated ZnS:Cu and PC (d) the interface of the spin-coated ZnS:Cu/PC structure. The enlarge SEM morphology of (e) spin-coated and (f) adhesive ZnS:Cu layers.

without an air interface between them. The ZnS:Cu layer exhibits a rough and porous surface morphology as shown in Fig. 2(d), which is beneficial for the capturing of incident beta particles and thus the reduction of backscattering. Fig. 2(e) and (f) exhibit enlarged SEM images of spin-coated and adhesive ZnS:Cu layers, respectively. It can be seen that the size of ZnS:Cu particles ranges from 0.5–5 μm, and the gel can be clearly seen mixed with the spin-coated ZnS:Cu particles.

A comparison of the energy distribution of beta particles deposited in adhesive and spin-coated ZnS:Cu layers and the energy deposition trend of each layer (100 nm) are shown in Fig. 3(a), which was simulated using the Monte Carlo N-Particle Transport Code (MCNP). It can be observed that beta particles incident into the spin-coated layer deposit around 18.3% of their energy in the 1 μm thick gel and 68.1% in the ZnS:Cu particles. The beta-energy deposition in the ZnS:Cu of adhesion layer is 79.8%, which is 11.65% higher than that in the spin-coated layer. The backscattering loss of the spin-coated layer is 13.6%, which is lower than that of the adhesive layer (~20.2%) due to the smaller scattering collision cross-section of the gel. Each red dot represents the energy deposition in a 100 nm thick layer, and the gel material is divided into 10 layers. As beta particles pass through the gel attached to the surface of ZnS:Cu particles, the energy deposition density decreases gradually with depth and then increases sharply at the interface of gel/ZnS:Cu. This is because that ZnS:Cu material has higher beta-energy absorbability than gel. Fig. 3(b) shows the radioluminescent spectrum of the spin-coated ZnS:Cu/PMMA and adhesive ZnS:Cu/BOPP layers. Since the transmittance of BOPP and PMMA substrates is approximately the same in the wavelength range of 400–650 nm, as shown in the inset of Fig. 3(b), the radioluminescence performance of both layers can be compared. It can be observed that under the same excitation of ^{63}Ni radioactive source, the adhesive ZnS:Cu layer exhibits a 40.6% higher radioluminescence intensity than that of the spin-coated one. This can be explained by the presence of non-luminescent gel material (as shown in Fig. 2(e)) in the spin-coated ZnS:Cu layer, which consumes part of the beta energy.

To further investigate the influence of the photon transport interface on RLIC performance, the reflectance and absorptance spectra at the PC interface of both structures were simulated with

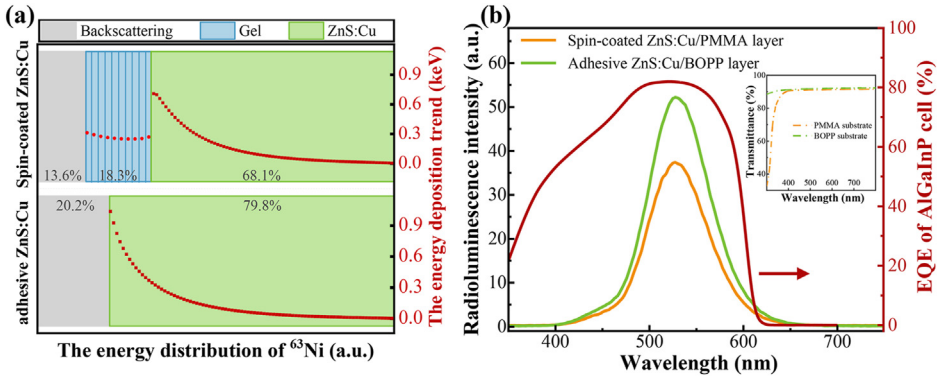

Fig. 3. (a) Comparison of the energy distribution and deposition trend of beta particles incident on the adhesive and spin-coated ZnS:Cu layers. (b) Radioluminescence spectrum of the spin-coated ZnS:Cu/PMMA and adhesive ZnS:Cu/BOPP structures, the EQE of the AlGaInP cell, and the transmittance of PMMA and BOPP substrates.

COMSOL, as shown in Fig. 4(a). Since photons are generated from ZnS:Cu (n = 2.4 at 520 nm) and directly incident into AlGaInP (n = 3.6 at 520 nm) with a positive refractive index gradient (from a low refractive index material to a high refractive index material), the ZnS:Cu/PC interface enables a low reflection loss of 2.6% in the wavelength range of 400–650 nm. As a result, the photons generated in the spin-coated ZnS:Cu layer can be fully absorbed by PC. In contrast, the photons generated in the adhesive ZnS:Cu layer will pass through the ZnS:Cu/BOPP interface and BOPP/PC interface with a thin air gap before being captured by the PC. Significant photon reflection occurs at both interfaces when photons are incident from high refractivity materials into low refractivity ones. It can be seen from Fig. 4(a) that the reflectance of the adhesive ZnS:Cu/BOPP/PC structure is higher than that of the spin-coated ZnS:Cu/PC one, and the average photon absorptivity available for PC is around 78.6%. Under the same ^{63}Ni radiation source, the *I–V* curves of all RLICs were measured, as shown in Fig. 4(b), and the electrical parameters were extracted and shown in Table 1. The electrical performance of each PC is slightly different, so 4 PCs (numbered #1 to #4) were used in the experimental comparison between the RLICs based on the adhesive ZnS:Cu/BOPP/PC (#1–1 to #4–1) and the spin-coated ZnS:Cu/PC (#1–2 to #4–2). It can be observed that the electrical output of all spin-coated ZnS:Cu/PCs is clearly improved, compared to the corresponding adhesive ZnS:Cu/BOPP/PCs with the same PC. The average increase in maximum power (P_{max}) and short circuit current (I_{sc}) reaches 30.2% and 18.7%, respectively. Although the energy deposition in ZnS:Cu grains of spin-coated layer decreases by 11.65% as shown in Fig. 3(a), the advantage of spin-coated structure is that it can be directly prepared on the surface of the photovoltaic cell and reduce transport loss. The spin-coated structure enables a higher photon-coupling-efficiency interface at the expense of a little beta energy.

The effect of the metal reflective film on RLIC performance was also investigated. COMSOL simulation was used to analyze the reflection and absorption of Ag, Al, and Ni metal films with different thicknesses in the wavelength range of 400–650 nm, which is the emission wavelength of ZnS:Cu, as shown in Fig. 5. It can be seen that the reflectance-limitation-thickness (RLT) of the Ag film is 100 nm, corresponding to an average reflectance of 98.7% and an average absorbance of only 1.2% at 400–650 nm (see Fig. 5(a)). The average reflectance of the Al film is 91.6% at 400–650 nm for an RLT of 50 nm (see Fig. 5(b)), which is slightly lower than that of the Ag film, and the average absorbance is as high as 8.3%. In contrast, the RLT of the Ni film is around 50 nm, corresponding to a minimum reflectance of 64% at 400 nm. The reflectance gradually increases to a value of 89% at 650 nm with an increase in wavelength (see Fig. 5(c)). This results in an average reflectivity of the Ni film of around 81.5% at 400–650 nm. The experimental results indicate that a 100 nm thick Ag film is the optimum selection for enhancing the reflection of fluorescence excited by beta radiation. However, the metal reflective film will result in beta energy loss through absorption and backscattering, and thus there is a trade-off between fluorescence reflection and beta energy loss, which depend on the thickness of the metal film.

In order to experimentally investigate the effect of the metal reflective film on the optical performance of radioluminescent structures, 100 nm thick Ag, Al, and Ni films and a 50 nm thick Ni film were prepared on the spin-coated ZnS:Cu/PMMA samples. PL spectra were used to assess the influence of the metal reflective film on fluorescence emission. A schematic diagram of PL spectra measurement is shown in the inset of Fig. 6(a). An ultraviolet (UV) light incident on the PMMA substrate at a 45-degree angle was used to excite the fluorescence of ZnS:Cu layer, which could be detected from another degree. The UV-excitation in the current measurement condition cannot completely simulate beta-excitation, but it does not affect the qualitative assessment of the metal reflective film on the ZnS:Cu layer. Fig. 6(a) shows the PL spectrum of spin-coated ZnS:Cu/PMMA samples without and with metal films. The ZnS:Cu/PMMA structure without a metal film shows the lowest PL intensity among all samples, implying the existence of energy loss due to backward light emission. It can be observed from Fig. 6(a) that the PL intensity increases with the use of a metal film. Compared to the PL intensity of the ZnS:Cu/PMMA structure without a metal film, the PL intensity of the ZnS:Cu/PMMA structure with 100 nm thick Ag, Al, and Ni films increases by 36.2%, 29.6%, and 14.3%, respectively, while a 50 nm thick Ni film only leads to a 7.5% improvement in PL intensity. Although simulation results show that the reflectance and absorbance of Ni film at 50 nm and 100 nm are the same, the 100 nm Ni film enables a higher PL intensity of around 7% than the 50 nm Ni film in experiments. It indicates that the actual reflectance of a metal film is positively related to its thickness within a limited range. In addition, it was also found that the peak wavelength of the PL spectrum has a slight redshift (5 nm) when using a metal film. This could be attributed to the excitation of surface plasmon polaritons (SPPs) on the metal film on the phosphor layer [34]. Since the PL peak is completely covered by the EQE spectra (as shown in Fig. 3(b)), this slight wavelength shift has no influence on photoelectric conversion of devices. The experimental result confirms that reflection from a metal reflective film covered on the phosphor layer enhances luminescence intensity by reflecting backward photons.

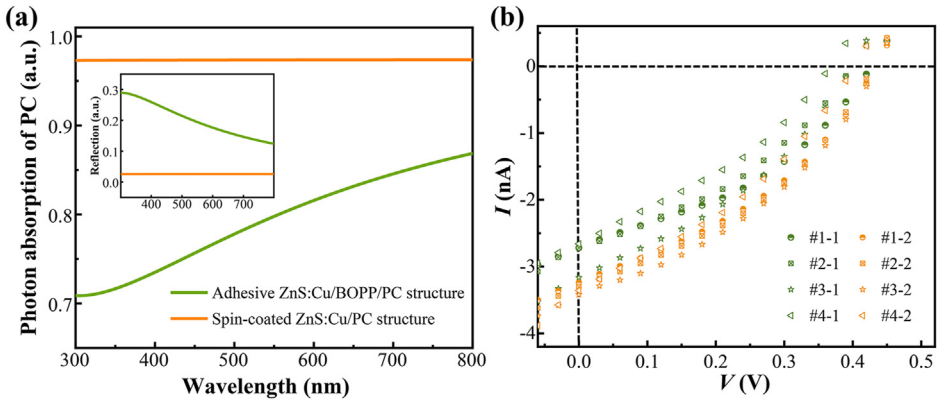

Fig. 4. (a) Absorption spectrum of PC with adhesive ZnS:Cu/BOPP/PC structure and spin-coated ZnS:Cu/PC structure, and the reflection of the photon transport process. (b) *I–V* curves of RLICs based on adhesive ZnS:Cu/BOPP/PC structures and spin-coated ZnS:Cu/PC integrated structures.

Table 1
Electrical parameters of RLICs based on adhesive ZnS:Cu/BOPP/PC structure and spin-coated ZnS:Cu/PC structure.

Adhesive ZnS:Cu/BOPP/PC	P_{max} (nW)	I_{sc} (nA)	V_{oc} (V)	*FF*	Spin-coated ZnS:Cu/PC	P_{max} (nW)	I_{sc} (nA)	V_{oc} (V)	*FF*
#1−1	0.45	2.71	0.43	0.39	#1−2	0.52	3.24	0.44	0.37
#2−1	0.41	2.71	0.40	0.38	#2−2	0.54	3.30	0.43	0.38
#3−1	0.45	3.19	0.40	0.35	#3−2	0.56	3.42	0.44	0.37
#4−1	0.33	2.65	0.37	0.34	#4−2	0.47	3.36	0.40	0.35

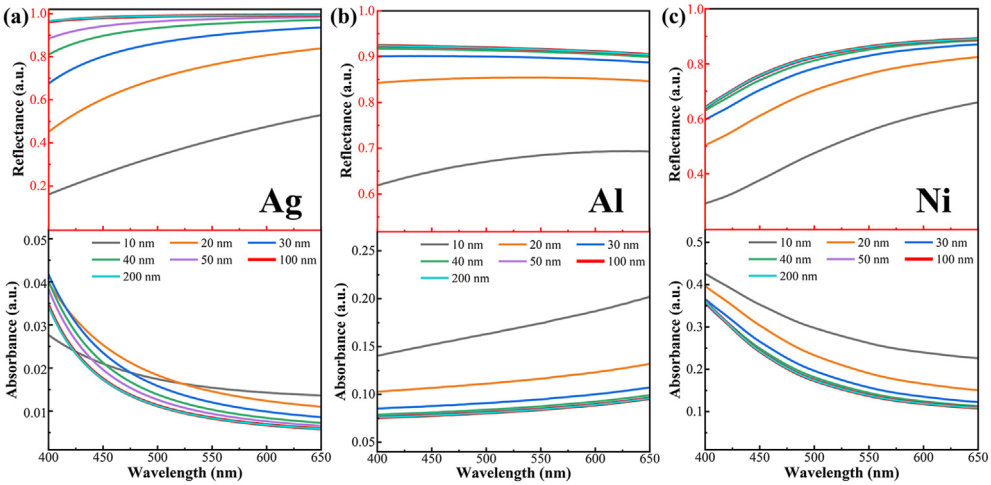

Fig. 5. Reflectance and absorbance of (a) Ag, (b) Al, and (c) Ni film with different thickness.

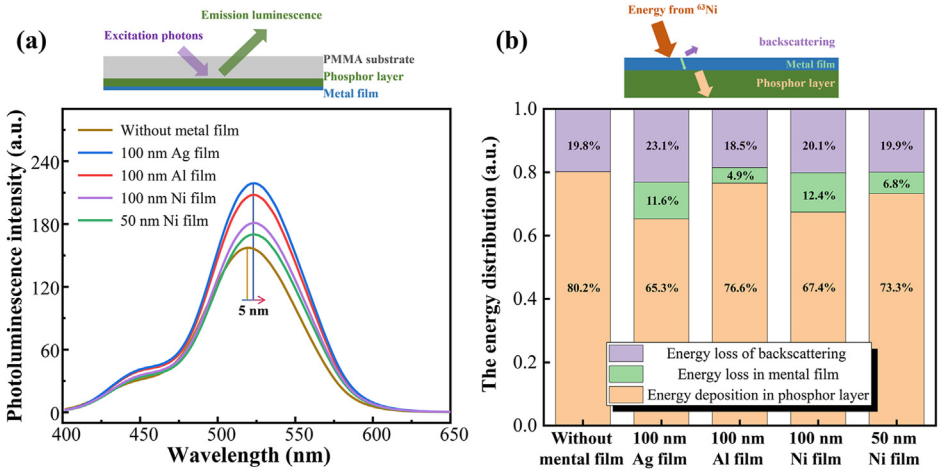

Fig. 6. (a) PL spectrum of the spin-coated ZnS:Cu/PMMA samples without and with metal films. (b) Simulated energy distribution of beta energy incident on ZnS:Cu layers without and with metal films.

Fig. 6(b) shows the disturbance of the metal film on incident beta particles, allowing for the calculation of energy deposition in the phosphor layer, energy in the metal film, and backscattering energy. Without using a metal reflective film, the energy loss of incident beta energy is around 19.8%, which is entirely attributed to backscattering from the surface of the ZnS:Cu layer. When using a 100 nm thick Ag film, absorption and backscattering energy losses reach 11.7% and 23.1%, respectively. In contrast, absorption and backscattering energy losses for a 100 nm thick Al film are 4.9% and 18.5%, respectively. Due to the fact that Al has a lower atomic weight than Ag, and thus the energy loss of Al induced by the interaction between beta particles and Al atoms, is lower than that of Ag. The effect of Ni film thickness on electron backscattering is not significant. The backscattering energy loss of a 50 nm thick Ni film is approximately equal to that of a 100 nm thick Ni film, with energy losses reaching 19.9% and 20.1%, respectively. However, the absorption energy loss of a 50 nm thick Ni film reaches 6.8%, which is slightly higher than half that of a 100 nm thick Ni film. As seen in Fig. 6(b), beta energy deposition in the ZnS:Cu layer without a reflective film reaches 80.2%, which is the highest compared to that with a reflective film. Among all structures with a metal film, the 100 nm thick Al film enables the maximum beta energy deposition with 76.6% in the ZnS:Cu layer.

RLICs based on spin-coated ZnS:Cu/PCs with different metal reflective films (100 nm thick Ag, Al, and Ni films, and a 50 nm Ni film) were assembled. An RLIC without any metal film was also assembled for performance comparison with the above devices. Fig. 7 shows the *I*−*V* and *P*−*V* characteristics of RLICs based on spin-

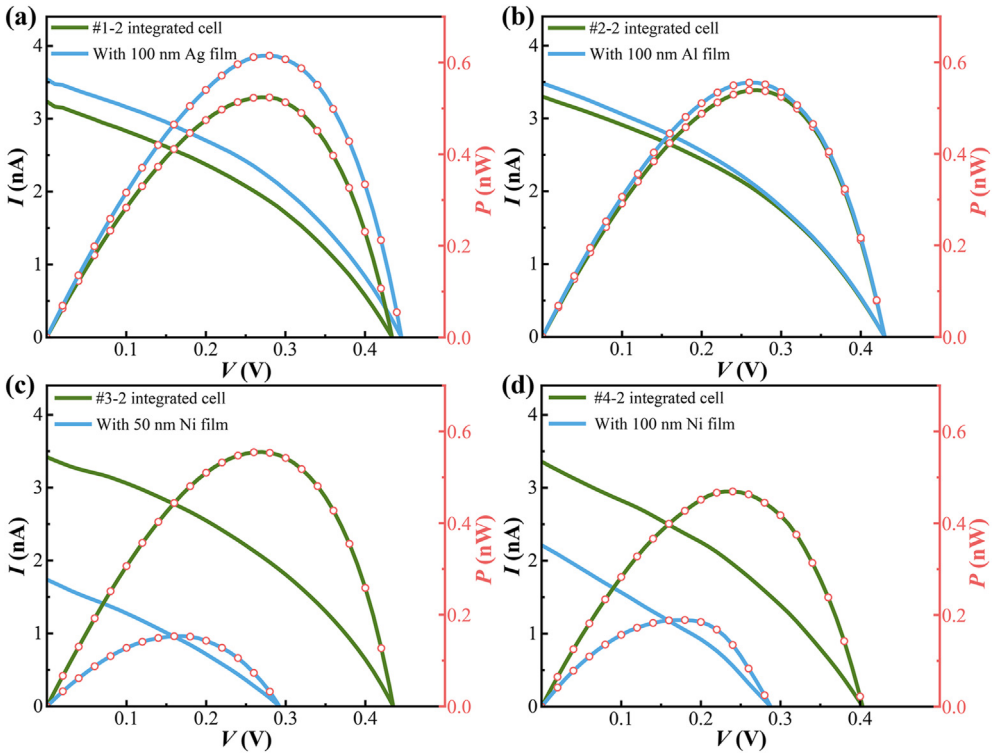

Fig. 7. *I–V* and *P–V* characteristics of the spin-coated ZnS:Cu/PC without a metal film and with (a) 100 nm Ag film, (b) 100 nm Al film, (c) 50 nm Ni film, and (d) 100 nm Ni film.

coated ZnS:Cu/PC with and without metal film, and the electrical parameters are shown in Table 2. It can be seen that RLICs with Ag and Al reflective films produce a larger output power than those without a metal reflective film. The Ag film enables the highest 17.2% increase in P_{max} compared to other metal films (see Fig. 7(a)), which is consistent with PL measurement results. However, the Al reflective film is not as effective as the Ag film, with only a 3.0% increase in P_{max} (see Fig. 7(b)). This could be due to the relatively lower reflectance and higher absorbance of Al compared to Ag film, as the simulation results shown in Fig. 5. In contrast, 50 nm and 100 nm thick Ni films lead to a significant 72.4% (see Fig. 7(c)) and 59.7% (see Fig. 7(d)) reduction in P_{max} compared to devices without a metal film, respectively. It is considered that the significant decline in electrical performance after using Ni film should be attributed to the serious absorption and relatively low beta energy deposition in the ZnS:Cu layer when beta particles pass through the Ni film. Therefore, Ni metal is not suitable as a reflective film on the phosphor layer nor as a radioactive layer. In contrast, a 100 nm thick Ag metal film is the optimal choice for enhancing the electrical output.

In comparison with previous work using adhesive ZnS:Cu layers ($\eta_{Ni\text{-}63}$ = 0.64% under radioisotope source excitation and $\eta_{electron\ beam}$ = 0.87% under electron beam excitation) [25], this work proposes using an Ag/spin-coated ZnS:Cu/PC structure to improve the electrical performance of RLICs, which can achieve an increase in output power as high as 52.6% compared to the adhesive ZnS:Cu/BOPP/PC structure. It is expected to achieve a maximum η (^{63}Ni) of 0.98% and a maximum η (electron beam) of 1.33%.

Table 2
Electrical parameters of RLICs based on spin-coated ZnS:Cu/PCs with metal reflective films.

Metal reflective film	P_{max} (nW)	I_{sc} (nA)	V_{oc} (V)	*FF*
#1−2 with 100 nm Ag	0.62	3.55	0.45	0.39
#2−2 with 100 nm Al	0.56	3.49	0.43	0.37
#3−2 with 50 nm Ni	0.15	1.74	0.29	0.30
#4−2 with 100 nm Ni	0.19	2.21	0.29	0.29

4. Conclusion

In conclusion, this study presents a ^{63}Ni-based RLIC with enhanced photon transport interfaces to improve the energy coupling of beta-excited fluorescence to electricity. Compared to conventional RLICs based on adhesive ZnS:Cu/BOPP/PC structures, an improved design is suggested in which the ZnS:Cu/PC integrated structure is proposed to reduce the reflection of interfaces and enhance photon coupling efficiency, and a metal reflective film is prepared on the ZnS:Cu layer to reflect radioluminescence towards the PC. It is verified that introducing a transparent substrate (such as BOPP or PMMA) between the ZnS:Cu layer and PC can result in high fluorescence loss of around 21.4% due to refractive index mismatch at transport interfaces. Furthermore, the metal film on the phosphor layer to reflect the backward emission of photons is proved to be effective. The optimal design of Ag, Al and Ni metal film thickness on radioluminescent performance and fluorescence reflection were studied through MC and COMSOL simulations. A 100 nm thick Ag film is suggested as the optimal choice for balancing fluorescence reflection and beta energy loss, with P_{max} = 0.62 nW, I_{sc} = 3.55 nA and V_{oc} = 0.45 V under beta radiation of ^{63}Ni. It is demonstrated that an RLIC using an Ag (100 nm)/spin-coated ZnS:Cu/PC structure can achieve an increase of 52.6% in output power compared to the conventional structure RLICs with adhesive ZnS:Cu/BOPP/PC structure. The fluorescence backward reflection and refractivity matching at interfaces are responsible for the enhancement of photon transport.

Declaration of competing interest

The authors declare that they have no known competing financial interests or personal relationships that could have appeared to influence the work reported in this paper.

Acknowledgements

This work was supported by the National Key Research and Development Program of China (No. 2022YFB1903200), the National Natural Science Foundation of China (Nos. 12175190, U2241284 and 12005101), the Natural Science Foundation of Fujian Province, China (No. 2022J02006).

References

[1] M.A. Prelas, L.W. Charles, L.W. Matthew, D.L. Eric, J.S. Robert, A.W. Denis, A review of nuclear batteries, Prog. Nucl. Energy 75 (2014) 117–148, https://doi.org/10.1016/j.pnucene.2014.04.007.

[2] A.S. Bykov, M.D. Malinkovich, I.V. Kubasov, A.M. Kislyuk, D.A. Kiselev, S.V. Ksenich, R.N. Zhukov, A.A. Temirov, M.V. Chichkov, A.A. Polisan, Yu.N. Parkhomenko, Application of radioactive isotopes for beta-voltaic generators, Russ. Microelectron. 46 (2017) 527–539, https://doi.org/10.1134/S1063739717080054.

[3] A.A. Krasnov, S.A. Legotin, Advances in the development of betavoltaic power sources (A review), Instrum. Exp. Tech. 63 (2020) 437–452, https://doi.org/10.1134/S0020441220040156.

[4] C.L. Zhou, J.S. Zhang, X. Wang, Y.S. Yang, P. Xu, P.X. Li, L. Zhang, Z.Y. Chen, H.R. Feng, W.W. Wu, Betavoltaic cell: the past, present, and future, ECS J. Solid State Sci. Technol. 10 (2) (2021) 27005, https://doi.org/10.1149/2162-8777/abe423.

[5] M.L. Terranova, Nuclear batteries:Current context and near-term expectations, Int. J. Energy Res. 46 (14) (2022) 19368–19393, https://doi.org/10.1002/er.8539.

[6] M.G. Spencer, T. Alam, High power direct energy conversion by nuclear batteries, Appl. Phys. Rev. 6 (3) (2019) 31305, https://doi.org/10.1063/1.5123163.

[7] S. Kumar, Atomic batteries: energy from radioactivity, J. Nucl. Ene. Sci. Power Generat. Technol. 1511 (2016) 7427, https://doi.org/10.4172/2325-9809.1000144.

[8] H. Moayedi, S. Hajibaba, H. Afarideh, M. Ghergherehchi, M. Mohamadian, Optimization of beta radioluminescent batteries with different radioisotopes: a theoretical study, Nucl. Sci. Eng. 195 (6) (2021) 614–625, https://doi.org/10.1080/00295639.2020.1848199.

[9] T. Jiang, Z. Xu, H. Wang, Z. Yuan, K. Liu, X. Tang, Research on output power of radio-voltaic nuclear battery, in: 2020 Asia Energy and Electrical Engineering Symposium, 2020, pp. 763–766, https://doi.org/10.1109/AEEES48850.2020.9121369.

[10] X. Li, J. Chen, D. Yang, X. Chen, D. Geng, L. Jiang, Y. Wu, C. Meng, H. Zeng, Mn^{2+} induced significant improvement and robust stability of radioluminescence in $Cs_3Cu_2I_5$ for high-performance nuclear battery, Nat. Commun. 12 (1) (2021) 3879, https://doi.org/10.1038/s41467-021-24185-7.

[11] J.T. Jarrell, N. Cherepy, Z. Seeley, E. Swanberg, L. Voss, C. Frye, M. Stoyer, R. Henderson, R. Nikolic, Radiation hardness of polycrystalline ceramic scintillators for radioisotope batteries, Hard X-Ray, Gamma-Ray, and Neutron Detector Physics XXIV 12241 (2022) 156–165, https://doi.org/10.1117/12.2635787.

[12] Y. He, Z. Xu, H. Wang, M. Bian, Y. Liu, X. Tang, Enhanced radioluminescence and improved radioluminescent nuclear battery output performance more than 50% with SiO_2 nanosphere coating, J. Lumin. 255 (2023) 119600, https://doi.org/10.1016/j.jlumin.2022.119600.

[13] R. Gao, R. Chen, P. Wan, X. Ouyang, Q. Lei, Q. Deng, X. Guan, G. Niu, J. Tang, W. Chen, Z. Liu, X.P. Ouyang, L. Liu, High efficiency formamidinium-cesium perovskite-based radio-photovoltaic cells, Energy Environ. Mater. (2022) e12513, https://doi.org/10.1002/eem2.12513.

[14] D. Yang, Z. Xu, C. Gong, L. Su, X. Li, X. Tang, D. Geng, C. Meng, F. Xu, H. Zeng, Armor-like passivated $CsPbBr_3$ quantum dots: boosted stability with hand-in-hand ligands and enhanced performance of nuclear batteries, J. Mater. Chem. 9 (13) (2021) 8772–8781, https://doi.org/10.1039/d0ta12365j.

[15] A. Sharma, J.M. Melancon, S.G. Bailey, S.R. Zivanovic, Betavoltaic cells using P3HT semiconductive conjugated polymer, IEEE Trans. Electron. Dev. 62 (7) (2015) 2320–2326, https://doi.org/10.1109/TED.2015.2434852.

[16] M. Sychov, A. Kavetsky, G. Yakubova, G. Walter, S. Yousaf, Q. Lin, D. Chan, H. Socarras, K. Bower, Alpha indirect conversion radioisotope power source, Appl. Radiat. Isot. 66 (2) (2008) 173–177, https://doi.org/10.1016/j.apradiso.2007.09.004.

[17] T. Jiang, Z. Xu, X. Tang, Z. Yuan, H. Wang, M. Bian, Comparison and study of the preparation methods for phosphor layer in nuclear battery, Int. J. Energy Res. 45 (8) (2021) 11712–11720, https://doi.org/10.1002/er.5526.

[18] C.L. Weaver, R.J. Schott, M.A. Prelas, D.A. Wisniewski, J.B. Rothenberger, E.D. Lukosi, K. Oh, Radiation resistant PIDECα cell using photon intermediate direct energy conversion and a ^{210}Po source, Appl. Radiat. Isot. 132 (2018) 110–115, https://doi.org/10.1016/j.apradiso.2017.11.026.

[19] K.K. Prudchenko, I.A. Tolkachev, E.A. Silantieva, E.V. Kontrosh, Investigation of the characteristics of a radioisotope source based on a $(Y)PO_4/(^{238}Pu)$ self-glowing crystal and an $Al_xGa_{1-x}As/GaAs$ photovoltaic converter, J. Phys.: Conf. Ser. 2103 (2021) 12195, https://doi.org/10.1088/1742-6596/2103/1/012195.

[20] A.A. Kukinov, T.V. Balashova, B.S. Kaverin, S. Yu Bukhvalova, A.N. Trufanov, M.N. Bochkarev, Models of radiovoltaic batteries based on organo-lanthanide complexes, Radiat. Phys. Chem. 194 (2022) 110000, https://doi.org/10.1016/j.radphyschem.2022.110000.

[21] C. Zhao, J. Ren, L. Lei, F. Liao, X. Shi, D. Zhou, K. Liu, Y. Zhao, Tenfold efficiency improvement of x-ray radioluminescent batteries basing on GAGG: Ce single crystal scintillators, Appl. Phys. Lett. 119 (2021) 223901, https://doi.org/10.1063/5.0073048.

[22] C. Zhao, J. Ren, L. Lei, F. Liao, K. Liu, Y. Zhao, X-ray radioluminescent battery with near milliwatt output power using CsI: Tl single crystal scintillator, Appl. Phys. Lett. 121 (2022) 123906, https://doi.org/10.1063/5.0109011.

[23] H. Lee, M. Yim, Examination of scintillator-photovoltaic cell-based spent fuel radiation energy conversion for electricity generation, Prog. Nucl. Energy 94 (2017) 46–54, https://doi.org/10.1016/j.pnucene.2016.10.004.

[24] M. Yoneyama, J. Kataoka, M. Arimoto, T. Masuda, M. Yoshino, K. Kamada, A. Yoshikawa, H. Sato, Y. Usuki, Evaluation of GAGG: Ce scintillators for future space applications, J. Instrum. 13 (2) (2018) P02023, https://doi.org/10.1088/1748-0221/13/02/P02023.

[25] T. Jiang, Z. Xu, C. Meng, Y. Liu, X. Tang, In-depth analysis of the internal energy conversion of nuclear batteries and radiation degradation of key materials, Energy Technol. 8 (2020) 2000667, https://doi.org/10.1002/ente.202000667.

[26] R. Walton, C. Anthony, M. Ward, N. Metje, D.N. Chapman, Radioisotopic battery and capacitor system for powering wireless sensor networks, Sensor Actuat. A-Phys. 203 (2013) 405–412, https://doi.org/10.1016/j.sna.2013.09.010.

[27] M.S. Litz, J.A. Russo, D. Katsis, Tritium-powered radiation sensor network, Chemical, Biological, Radiological, Nuclear, and Explosives (CBRNE) Sensing XVII 9824 (2016) 243–254, https://doi.org/10.1117/12.2222177.

[28] Z. Xu, Y. Liu, Z. Zhang, W. Chen, Z. Yuan, K. Liu, X. Tang, Enhanced radioluminescent nuclear battery by optimizing structural design of the phosphor layer, Int. J. Energy Res. 42 (4) (2018) 1729–1737, https://doi.org/10.1002/er.3982.

[29] R.K. Yürük, H. Tütüncüler, Investigation of the effect of beta source and phosphors on photovoltaic cells, AIP Conf. Proc. 1815 (2017) 40002, https://doi.org/10.1063/1.4976371.

[30] Y. Lei, Y. Yang, G. Li, Y. Liu, J. Xu, X. Xiong, S. Luo, T. Peng, Demonstration and aging test of a radiation resistant strontium-90 betavoltaic mechanism, Appl. Phys. Lett. 116 (2020) 153901, https://doi.org/10.1063/1.5140780.

[31] Z. Xu, Z. Jin, X. Tang, Y. Liu, X. Guo, C. Peng, H. Wang, Designing performance enhanced nuclear battery based on the Cd-109 radioactive source, Int. J. Energy Res. 44 (2020) 508–517, https://doi.org/10.1002/er.4958.

[32] J. Russo, M. Litz, W. Ray, B. Smith, R. Moyers, A radioluminescent nuclear battery using volumetric configuration: ^{63}Ni solution/ZnS:Cu,Al/InGaP, Appl. Radiat. Isot. 130 (2017) 66–74, https://doi.org/10.1016/j.apradiso.2017.09.018.

[33] Z. Xu, X. Tang, L. Hong, Y. Liu, D. Chen, Development of a beta radioluminescence nuclear battery, Nucl. Sci. Tech. 25 (4) (2014) 40603, https://doi.org/10.13538/j.1001-8042/nst.25.040603.

[34] M.A. Noginov, G. Zhu, M. Mayy, B.A. Ritzo, N. Noginova, V.A. Podolskiy, Stimulated emission of surface plasmon polaritons, Phys. Rev. Lett. 101 (22) (2008) 226806, https://doi.org/10.1103/PhysRevLett.101.226806.